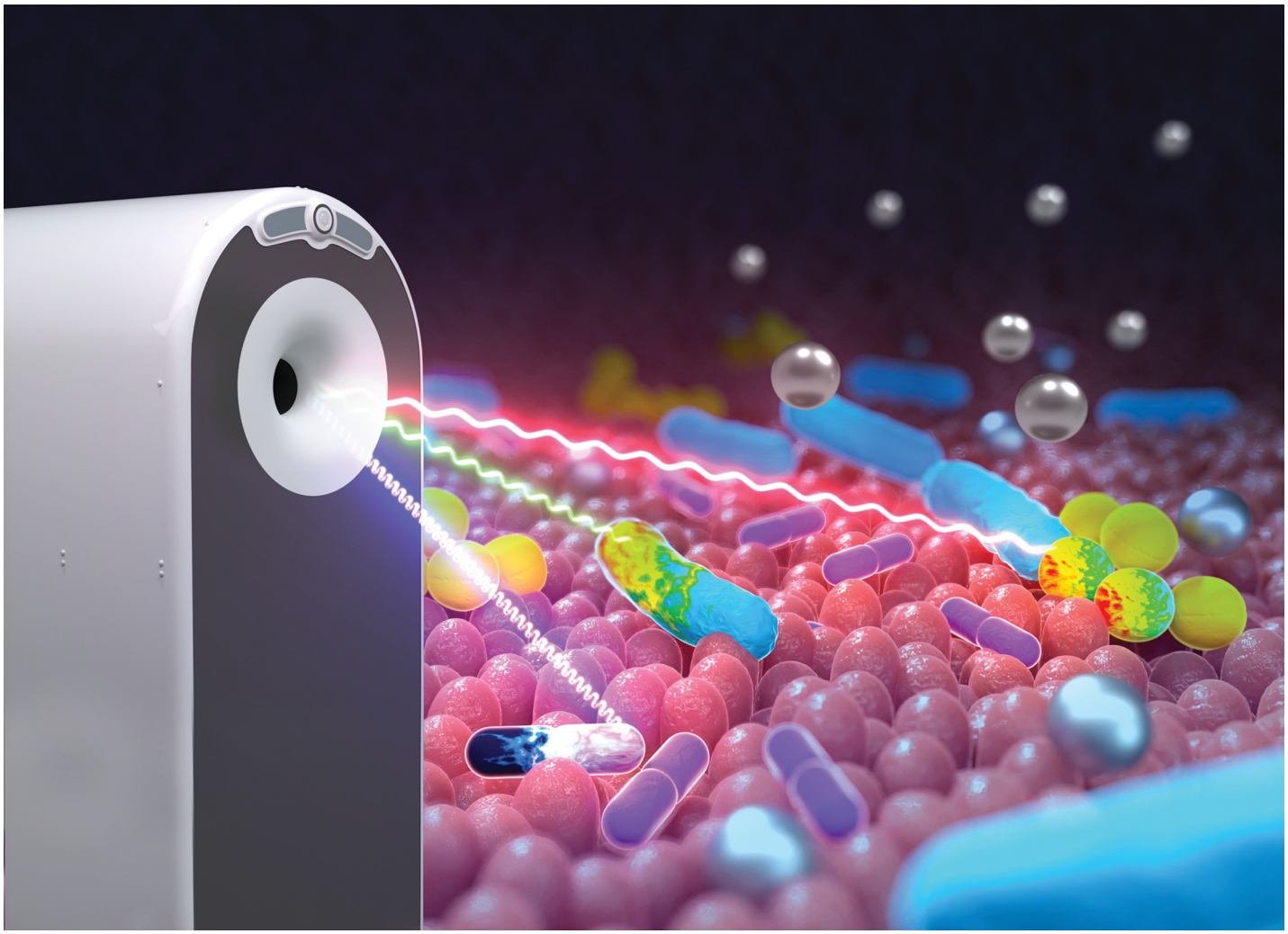

Highlighting research from Professor Dipanjan Pan's laboratory, University of Maryland Baltimore and University of Maryland Baltimore County.

Hitchhiking probiotic vectors to deliver ultra-small hafnia nanoparticles for 'Color' gastrointestinal tract photon counting X-ray imaging

We report an approach to deliver ultra-small hafnia nanodots to gastrointestinal tract. The nanodots were packaged inside orally ingestible probiotic vectors to achieve enhanced nano-bio-interfacing capacity while offering an alternative to conventional barium meal. Photon counting spectral computed tomographic imaging was performed to see through the GI tract in 'color' as being differentiated by the favorable specific K-edge binding energy of Hf. In these never-before-seen images, Hf is clearly delineated in the lining of the esophagus and differentiated from lipids, soft tissue, and the other metals (from food intake).

As featured in:

See Dipanjan Pan *et al.*, *Nanoscale Horiz.*, 2022, **7**, 533.

ROYAL SOCIETY OF CHEMISTRY

rsc.li/nanoscale-horizons

Registered charity number: 207890

Nanoscale Horizons

ROYAL SOCIETY OF CHEMISTRY

COMMUNICATION

View Article Online
View Journal | View Issue

Cite this: *Nanoscale Horiz.*, 2022, 7, 533

Received 30th November 2021,
Accepted 14th March 2022

DOI: 10.1039/d1nh00626f

rsc.li/nanoscale-horizons

Hitchhiking probiotic vectors to deliver ultra-small hafnia nanoparticles for 'Color' gastrointestinal tract photon counting X-ray imaging†

Fatemeh Ostadhossein,‡[ab] Parikshit Moitra,‡[c] Nivetha Gunaseelan,[cd] Michael Nelappana,[a] Chiara Lowe,[e] Mahdieh Moghiseh,[ef] Anthony Butler,[efghi] Niels de Ruiter,[efgi] Harish Mandalika,[fgi] Indu Tripathi,[a] Santosh K. Misra[a] and Dipanjan Pan *[abcdj]

Gastrointestinal (GI) tract is one of the hard-to-reach target tissues for the delivery of contrast agents and drugs mediated by nanoparticles due to its harsh environment. Herein, we overcame this barrier by designing orally ingestible probiotic vectors for 'hitchhiking' ultrasmall hafnia (HfO_2) (~1–2 nm) nanoparticles. The minute-made synthesis of these nanoparticles is accomplished through a simple reduction reaction. These nanoparticles were incubated with probiotic bacteria with potential health benefits and were non-specifically taken up due to their small size. Subsequently, the bacteria were lyophilized and packed into a capsule to be administered orally as the radiopaque contrast agents for delineating the GI features. These nano-bio-hybrid entities could successfully be utilized as contrast agents *in vivo* in the conventional and multispectral computed tomography (CT). We demonstrated in 'color' the accumulated nanoparticles using advanced detectors of the photon counting CT. The enhanced nano-bio-interfacing capability achieved here can circumvent traditional nanoparticle solubility and delivery problems while offering a patient friendly approach for GI imaging to replace the currently practiced barium meal.

New concepts

The gastrointestinal tract (GI) is one of the hard-to-reach areas for imaging and the clinical method for the interrogation of information is limited to Barium meal using CT imaging. However, this method has low patient compliance due to the unpleasant taste of the contrast agent taken orally. Herein, we introduced a biomimetic capsule-packed contrast agent material based on patient friendly probiotic bacteria for the color delineation of GI tract. The ultrasmall (1–2 nm) HfO_2 nanoparticles (NPs) were taken up by bacteria *via* a passive route and subsequently the bacteria were freeze-dried. The NPs were fabricated on Gram-scale in a minute-made synthesis. We utilized these entities in photon counting spectral CT *in vivo* to see through the GI tract in color as being differentiated by the favorable specific K-edge binding energy of Hf. Since a photon-counting CT system employs a photon-counting detector (PCD) which registers the interactions of individual photons, the abundance of the contrast material, *i.e.*, Hf is clearly delineated in the lining of the esophagus and differentiated from lipids, soft tissue, and the presence of other metals evidently present from the food intake. Overall, we demonstrated for the first time that tiny nanometric scale hafnium can be microencapsulated within a probiotic system and delivered successfully for K-edge weighted imaging.

Introduction

For diagnostic probing of the stomach, traditionally, high-attenuation X-ray-based contrast agents have been used to enhance and distend the gastrointestinal (GI) tract.[1,2] Intravenously administered positive contrast agents have an X-ray attenuation greater than that of water.[3] Although these agents are generally well-tolerated and effective in producing good

[a] *Department of Bioengineering, University of Illinois at Urbana-Champaign, 611 West Park Street, Urbana, IL, USA. E-mail: dipanjan@som.umaryland.edu*
[b] *Beckman Institute of Advanced Science and Technology, 405 N. Mathews M/C 251, Urbana, IL 61801-2325, USA*
[c] *Departments of Diagnostic Radiology and Nuclear Medicine and Pediatrics, University of Maryland Baltimore, 670 W Baltimore St., Baltimore, Maryland, 21201, USA*
[d] *Department of Chemical, Biochemical and Environmental Engineering, University of Maryland Baltimore County, Baltimore, Maryland, 21250, USA*
[e] *University of Otago Christchurch, Christchurch, New Zealand*
[f] *MARS Bioimaging Limited, Christchurch, New Zealand*
[g] *University of Canterbury, Christchurch, New Zealand*
[h] *European Organization for Nuclear Research (CERN), Geneva, Switzerland*
[i] *Human Interface Technology Laboratory New Zealand, University of Canterbury, Christchurch, New Zealand*
[j] *Department of Materials Science and Engineering, 201 Materials Science and Engineering Building, 1304 W. Green St. MC 246, Urbana, IL 61801, USA*

† Electronic supplementary information (ESI) available: Detailed experimental section as well as XPS characterizations and more spectral CT data. See DOI: 10.1039/d1nh00626f

‡ The authors contributed equally.

gastric distention, the delineation of the GI tract and stomach is not optimal. Contrast agents administered by the oral route is the most convenient due to high patient compliance, less sterility limitations and the ease of scale up.[4–7] Contrast agents that are oil-dispersible produce satisfactory image contrast of the stomach wall but are not very pleasant when given orally. On the other hand, the poor bioavailability of drug administered through an oral route is a major drawback of the process.[8–12]

Engineered nanoparticles (NPs) delivered *via* biological entities can combine the benefit of precise control over synthetic procedures while leveraging the natural cell functions.[13–15] This approach can lay the foundation of 'nano-bio-hybrid materials' which can mimic the biological processes and enhance the bio-interfacing ability of the NPs.[16–18] A number of diseases are known to be originated from the dysregulation of innate immune system consisting of physical barriers (mucus layers and epithelia covering gastrointestinal and respiratory tracts) and molecules released by phagocytic cells, *e.g.* chemokines and cytokines.[19] Numerous studies have already been conducted to demonstrate the interaction of nanoparticles on the immune system influenced by the physicochemical properties of the nanoparticles such as solubility, size, shape and surface charge.[20–25] It was shown that neutrophils induced ROS production followed by the activation of NADPH oxidase after the exposure with different nanoparticles, especially inorganic nanoparticles (*e.g.* SiO_2, TiO_2, AgNPs, AuNPs, ZnO NPs *etc.*).[26] Several studies also demonstrated that small and cationic nanoparticles induced more inflammatory response than larger and anionic/neutral ones due to the formation of protein-corona on the nanoparticle surface mediated by the electrostatic interaction of the nanoparticles with negatively charged proteins.[27] This introduced release of various cytokines followed by different kinds of immune reactions under *in vivo* conditions. In some of the cases, the uptake of inorganic nanoparticles triggered a calcium flux inside cells and ROS production that induced NLRP3 inflammasome activation followed by stimulation of IL-1β maturation and liver inflammation.[28] Multiple studies further showed the ability of inorganic nanoparticles to induce DNA damage, increase oxidative stress, and initiate apoptosis under *in vitro* conditions.[29] The *in vivo* toxicity of the nanoparticles was also investigated on rodent models.[30] With this background, we believed that the as-prepared Hf nanoparticles might face difficulties in meeting *in vivo* biocompatibility criteria if gavage by its own. Hence, we conceived of introducing these hafnia nanoparticles hitchhiking probiotics which may be a reasonable alternative.

Nano-bio-hybrid carriers can therefore potentially be exploited in the GI tract imaging to circumvent the problems associated with the bare NPs exposure. Current GI tract imaging approaches relying on either the invasive endoscopic methods or the non-invasive imaging methods are not patient friendly.[31] For instance, in the omnipresent clinical method known as barium meal, the patient must ingest 100 ml of barium sulphate after 6–8 h of fasting while there are reports about unknown median lethal dose for this compound and potential false positive results.[3,32]

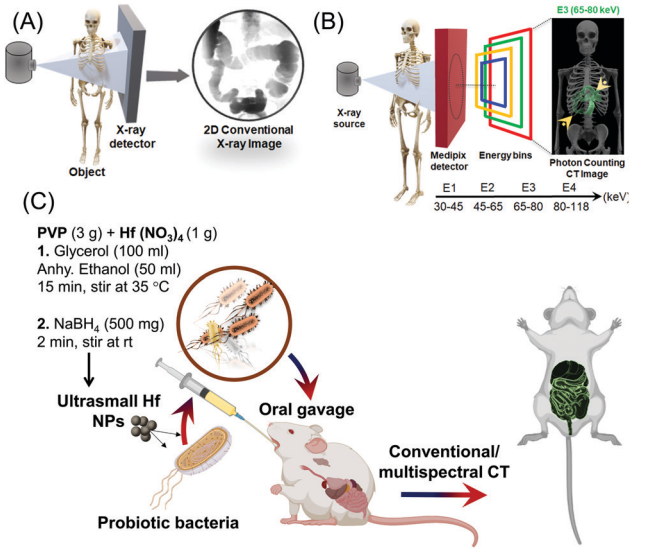

Fig. 1 (A) Schematic depiction of conventional 2D X-ray image formation; (B) schematic depiction of photon counting CT image formation where transmitted spectrum is divided by medipix detector into four energy bins (30–118 keV). The datasets are processed to provide 'color' images containing specific material decomposition images, *e.g.*, bone (calcium) and other k-edge metals, *e.g.*, Hf; (C) Schematic illustration for synthesizing and using ultra-small Hf NPs loaded in probiotics for the *in vivo* imaging of GI tract.

Spectral CT is an emerging technique where information is derived from photon-counting detectors that distinguish photon energies of individual photons.[33–35] The detected X-rays are divided into several energy windows to discriminate multiple materials based on their unique k-edge energies (Fig. 1A and B).[36] Photon counting CT (PCCT) imaging-based techniques are expected to offer lower radiation doses than conventional X-ray based techniques.[37–39] Researchers have used iodinated polymer nanoparticles for 'blood pool' contrast agent,[40] anti-plasma membrane Heat shock protein 70 (Hsp70) antibody functionalized gold nanoparticles for tumor-specific multimodal imaging,[41] multimodal nanocarrier probes for optical and nuclear imaging of macrophage cells,[42] hafnia nanodots for multi-color delineation of bone microdamage,[43] rhenium sulfide nanoparticles for gastrointestinal tract imaging *in vivo*,[44] gold nanoparticles to observe their biodistribution *in vivo*[45] and bi-diethylene triamine pentaacetate acid (Bi-DTPA) complex for *in vivo* high-performance CT and spectral CT imaging.[46]

Contrast agents for conventional CT employ elements that have much higher Z values than those found in the body, such as iodine, barium, gold, bismuth and so on. An intrinsic limitation of CT is its low sensitivity to contrast (limit of detection 10^{-3} M) compared with MRI (gadolinium chelate, 10^{-5} M) or nuclear based (10^{-9} M) techniques.[47,48] Photon counting CT has been proposed to encounter these issues and bring much needed improvement in sensitivity for CT imaging.[49–52] Elements with K-shell electron energies within the bandwidth of the incident X-ray spectrum can serve as K-edge contrast agents, and this range is generally considered to extend between iodine and bismuth on the periodic table of

elements. Hafnium has K-edge discontinuity well inside the energy regime and may become most relevant for medical X-ray imaging. Iodine (33.2 keV) and barium (37.4 keV), which are on the lower edge of the X-ray bandwidth, will be effective in rodents, but the effects of photon starvation and scattering occurring in patients may severely limit the utility of current clinically approved contrast agents for K-edge imaging applications. Only recently, dextran-coated cerium oxide nanoparticles has been used for noninvasive gastrointestinal tract imaging for inflammatory bowel disease.[53] These nanoparticles produced strong CT contrast in the colitis area of large intestine and gets cleared from the body within 24 h of administration.

Fig. S1 (ESI†) shows cross sectional CT images of serially diluted iodine-based contrast agents, suspended $BaSO_4$, and HfO_2 nanoparticles under similar experimental conditions and concentration (0.01 mmol ml^{-1}). As evident from the results, hafnium-based agents exhibited stronger contrast than iodine and barium. However, the benefit of using Hf will not be clear from conventional CT scanning as the test was performed at 80 keV. At this energy K-edge of iodine and barium would strongly influence their attenuation and the greater attenuation advantage of hafnium from its higher *Z*-value will be somewhat erased, with approximately equal attenuation from the two elements observed in practice.[54,55] The advantage of hafnium is truly translation in nature, where the contrast agents based on this metal will not be compromised by the photon starvation and scattering as is the case for contrast agents with low K-edge energy, *i.e.*, iodine and barium.

Herein, we report the rapid synthesis of ultra-small hafnia (HfO_2 NPs) whose delivery has been mediated by nonvirulent probiotic strains. The engineering of this nano-bio-hybrid was inspired by the gut-friendly probiotics.[56,57] This provided a biological basis for our attempt to deliver metallic contrast probes by shuttling or 'hitchhiking' the particles on probiotics. This reasoning led us to develop a prototype version of nano-bio-hybrid comprising probiotic-hitchhiking and metallic NPs. The hypothesized mechanism is that when probiotics are compressed through the GI tract, they transfer the NPs to the lining of the GI tract. We anticipate that this strategy will remarkably improve, generalize and may extend this early concept into producing a highly effective nanomedicine platform technology for GI diseases.

The synthesis of ultra-small hafnia (HfO_2 NPs) is based on nitrate reduction of Hf containing precursor (Hf nitrate) at room temperature which resulted in large scale minute-made fabrication of $\sim$2 nm HfO_2 nanodots stabilized by polyvinylpyrrolidone (PVP) (P-HfO_2 NPs) without utilizing any toxic organic solvents. The internalization of these NPs in probiotics ensued by simple incubation to offer a nano-bio-hybrid entity (bio-HfO_2) which was subsequently employed for the GI tract imaging using conventional and multispectral photon counting X-ray based imaging.[33,34,58]

Probiotics have the ability to colonize in the human GI tract and have been shown to confer therapeutic effects in several diseases such as the inflammatory bowel conditions and enteric infection.[59,60] In this context, we utilized two probiotic strains namely *Escherichia coli* (*E. coli*) Nissle 1917 and *Lactococcus lactis* (*L. lactis*) which can internalize and concentrate the HfO_2 NPs while they can withstand the rough GI condition to protect the cargo from leaching and degradation (Fig. 1C).

Hf has a strong X-ray attenuation coefficient and a well-positioned K-edge which makes it favorable as contrast agent in computed tomography (CT) and, in particular, in more advanced spectral CT technology.[61] Its high biocompatibility and X-ray sensitizing are exploited in 50 nm NBTXR3 HfO_2 NPs which is under clinical trials in Europe as radiosensitizer for the treatment of cancer.[62] Previously, we have accomplished the synthesis of sub 5 nm HfO_2 NPs *via* the sol–gel chemistry in nanoemulsion method to utilize for the specific differentiation and imaging of carious bacteria in complex dental biofilm.[61] while we exploited a modified version of these NPs for the sensitive detection of bone microdamages.[63] Others have concurrently reported the sol–gel chemistry followed by annealing, direct precipitation and microwave assisted hafnia NPs with sizes bigger than 15 nm.[64–66] All these methods entail the utilization of toxic reagents while they are tedious and time consuming. In this work, we present a large-scale, rapid synthesis of ultra-small, well-dispersed HfO_2 NPs.

The HfO_2 NPs were obtained based on reduction and stabilization method. In a typical synthesis, 3 g of polyvinyl pyrrolidine (PVP) and 1 g of $Hf(NO_3)_4$ were dissolved in 100 ml of glycerol and 50 ml of anhydrous ethanol (EtOH) with a magnetic stir bar at ambient temperature. Subsequently, 500 mg of $NaBH_4$ was added quickly to this solution and was allowed 2 min to form the P-HfO_2 NPs. Finally, the NPs were centrifuged and were washed several times with ethanol and water in turn and were dried under vacuum. The NPs were easily dispersed in water by brief tip sonication.

Transmission electron microscopy (TEM) indicated the formation of well-dispersed spherical NPs with the size distribution shown in Fig. 2Ai and ii. the average anhydrous diameter was calculated to be 2.13 ± 0.52 nm (Fig. 2B). The selected area diffraction pattern (SAED) is also shown in Fig. 2Aiii, where several diffraction spots and diffraction rings were identified implying the semi-crystalline nature of these ultra-small NPs. On the other hand, the height of P-HfO_2 NPs was measured with atomic force microscopy (AFM) and the average height was determined to be 0.9 ± 0.1 nm (Fig. 2C).

The crystal structure of the material was further investigated with powder X-ray diffraction and the peak pattern can be assigned to (ICDD Card No. 00-034-0104) associated with HfO_2 in monoclinic phase (Fig. 2F). Inductively coupled plasma–optical emission spectroscopy (ICP-OES) revealed that Hf percentage was 50.4 wt% while CHN analysis determined the C, H, N to be 4.05, 2.2, and 0.34 wt%, respectively. We characterized the amount of PVP coating with the aid of thermal gravimetric analysis (TGA) (Fig. 2E) where we observed a thermal event associated with the bound water in the sample. A second thermal event was starting from 200 °C attributed to PVP decomposition and the weight percentage was calculated to be 18.01% and afterwards the graph reached a plateau.

The UV-Vis absorbance spectrum is shown in Fig. 3A where a strong broad absorbance ranging from UV to NIR range can be

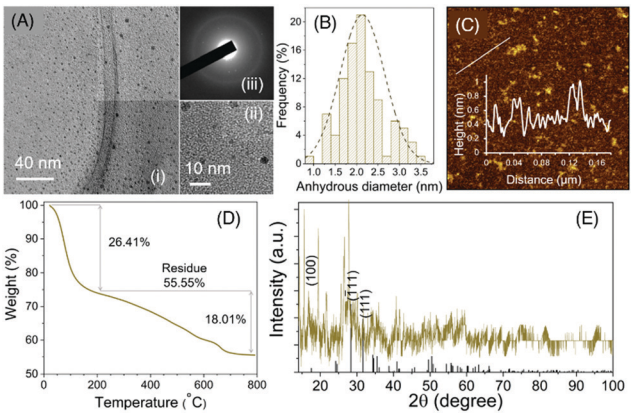

Fig. 2 (A) (i), (ii) HRTEM images of the NPs, (iii) SAED pattern of the NPs; (B) anhydrous size distribution of NPs from TEM; (C) AFM height distribution of the NPs; the inset shows the height profile along the indicated line; (D) TGA of NPs with two thermal events identified; (E) XRD pattern.

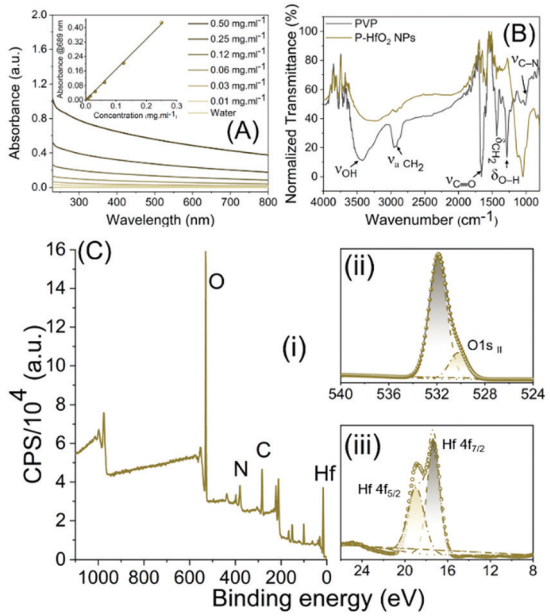

Fig. 3 (A) UV-Vis absorbance spectra of NPs at various concentrations, (B) FTIR spectra; (C) XPS spectra in (i) survey mode, (ii) O1s region and (iii) Hf 4f region.

noticed (Fig. 3A). In addition, the absorbance *vs.* concentration plot was constructed, and it could be seen that there is a linear relationship suggesting that the absorbance is not originating from scattering but rather from the innate absorbance from the NPs. To elucidate the chemical composition, we carried out Fourier transform infrared spectroscopy (FTIR) spectroscopy (Fig. 3B). For PVP, the peaks observed at 1019 cm^{-1} and 1281 cm^{-1} were attributed to C–N vibration, peak observed at 1435, 1655, 2953 cm^{-1} were related to CH_2 bending vibration, C═O stretching vibration in carbonyl, and asymmetric stretching vibration in CH_2, respectively. Moreover, the peak at 3420 cm^{-1} was attributed to OH stretching vibration while 899 cm^{-1} was related to breathing vibration of the pyrrolidone ring. In the spectrum of P-HfO_2 NPs, these peaks were preserved while the peak at 1655 cm^{-1} was shifted to 1637 cm^{-1} possibly due to the coordination of Hf ion and carbonyl oxygen.

We further analyzed the samples using X-ray photoelectron spectroscopy (XPS) which provides information on the surface functional groups. At first, the peak assignment for PVP was made (Fig. S2–S6, ESI†) where the peaks observed at 284.8, 285.80, and 287.49 eV in C1s (Fig. S5, ESI†) region could be correlated to C–C, C–N and C═O, respectively. On the other hand, the deconvolution of the peaks in the N1s region revealed the peak at 339.5 eV related to tertiary N (Fig. S4, ESI†) and finally the peaks of O1s at 531.0 eV was attributed to C═O in carboxyl (Fig. S3, ESI†). For P-HfO_2 NPs, we inspected Hf 4f region to identify Hf $4f_{7/2}$ and Hf $4f_{5/2}$ observed at 17.3 and 18.9 eV related to Hf in valence number of 4+ observed in HfO_2 (Fig. 3Ciii). The O1s peak at 530.2 eV can be correlated to O_{II} in (Fig. 3Cii) and peak at 531.9 eV could be related to organic C═O.

Having successfully synthesized and characterized these small NPs, we first investigated the dispersibility and stability of nanoparticles over time. It was observed that the time dependent increase in hydrodynamic diameter was quite insignificant at least up to six days and there was only minimal increase in size on the seventh day (Fig. S7, ESI†). It may be noted that the hydrodynamic diameter for the hafnia nanoparticles might be indicative of average size of the agglomerated particles which is found to be quite stable over time. Next, we examined their feasibility for the bio-interfacing application. We initially tested the cell compatibility of P-HfO_2 NPs with the bacteria which can act as the vectors for their transport. We, therefore, incubated *E. coli* Nissle with NPs to concentrations as high as 10 mg ml^{-1}. We subsequently carried out live/dead assay using BacLight™ bacterial viability kit which consists of two dyes; namely, SYTO9 and propidium iodide (PI) which determine the live and dead cells, respectively. The kit works based on the displacement of SYTO9 by PI when the bacterial cell membrane is damaged. The confocal images (Fig. 4A) revealed the comparable level of live bacteria identified by green compared to water treatment group without the damage to cell components. As shown in Fig. 4B, upon quantification, the ratio of live: dead cells are unchanged when increasing the concentration and there is no statistically significant difference among the groups. Interestingly, this ratio is maintained up to 10 mg ml^{-1} which is extremely high for conducting cell viability studies. This experiment has implication for CT imaging where the sensitivity of CT entails the application of contrast agents in mM range.

We further exposed the intestinal cells of human origin (Hs 1.Int cells (ATCC® CRL-7820™)) to determine the biocompatibility of HfO_2 NPs using metabolic MTT assay. Intestinal cells were adopted for this experiment due to the oral route of administration for GI tract imaging. It was observed that the ultrasmall hafnia nanoparticles are biocompatible in nature, even at very high concentration of 1 mg ml^{-1} of the particles (Fig. 4C). This indicated optimum biosafety of the synthesized NPs.

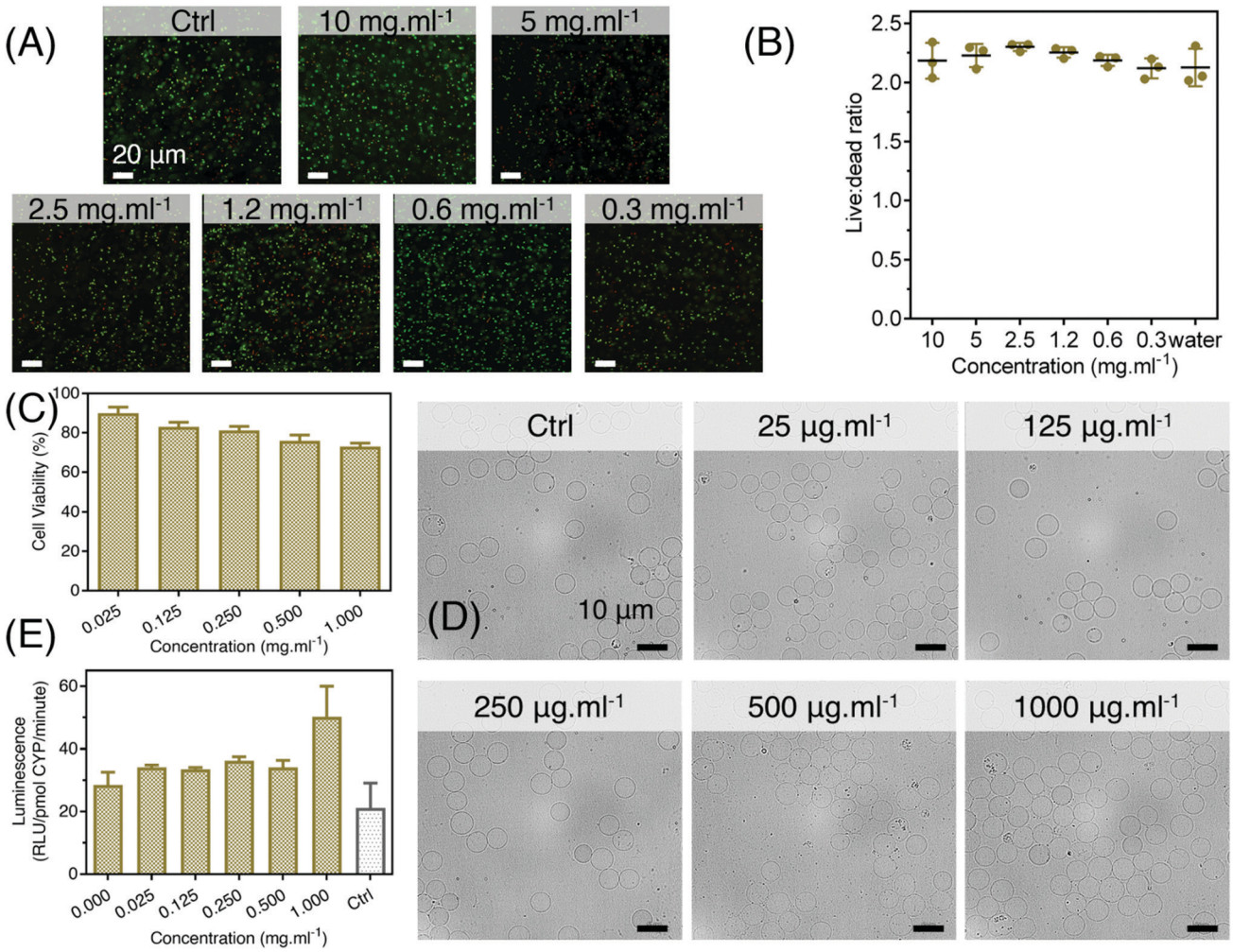

Fig. 4 *In vitro* application of probiotics incubated with P-HfO_2 NPs (A) live- dead fluorescent assay of *E. coli* Nissle incubated with NPs with concentration ranging from 0–10 mg ml^{-1}; (B) quantitative live dead results by plate reader; (C) MTT assay results on the intestinal cells; (D) the blood compatibility assay based on smearing showing no observable difference between control and the treated samples; (E) CYP3A4 metabolic assay at different concentration with a control of ketoconazole at 5 µM concentration.

In addition, the direct exposure of these NPs to blood is unlikely due to our administration method, it still presents a possible scenario in the case of GI bleeding, including hemorrhoids, peptic ulcers, and tearing or inflammation in the esophagus. With this mind, we further expanded our studies for the evaluation of hemocompatibility of P-HfO_2 NPs. Briefly, we incubated the NPs with freshly acquired rabbit blood and then carried out 'blood smear' assay to account for their morphological deformation. No obvious clumping or morphological abnormalities in blood cells were perceived in fresh rabbit blood treated with various concentrations of ultrasmall HfO_2 nanoparticles as compared with the control (untreated blood) as shown in Fig. 4D.

Ultimately, we evaluated the biosafety of the synthesized NPs by CYP3A4 assay. It is known that CYP3A4 are the most prevalent family of cytochrome P450 enzymes present in the liver and small intestine. The reduced activity of CYP3A4 enzyme is known to indicate slower metabolism of CYP3A4 substrates leading to an increase in substrate's *in vivo* concentration and thereby increased toxicity.[67] On the contrary, we observed insignificant change in CYP3A4 activity with the increase in P-HfO_2 NPs concentration. Moreover, there is a little positive cooperativity of the ultrasmall NPs with CYP substrates (Fig. 4E). This indicated that the ultrasmall HfO_2 NPs will introduce insignificant metabolic toxicity and thus will be safe under *in vivo* conditions.

Having established their cytocompatibility, we reasoned that P-HfO_2 NPs encapsulated in the probiotics (bio-HfO_2) can provide a safer and patient-friendly means for GI tract imaging. To this end, we incubated P-HfO_2 NPs with two probiotic types namely *L. lactis* and *E. coli* Nissle. As shown in the TEM images (Fig. 5C and D), the NPs are internalized by both strains of bacteria possibly due to their small size. No significant aggregation was noticed upon internalization by the bacteria (Fig. 5C inset). *L. lactis* is a Gram-positive bacterium while *E. coli Nissle* is a Gram-negative strain. Importantly, we noticed that after the incubation of NPs with these bacteria, the cell wall structure is well-preserved as shown in TEM images.

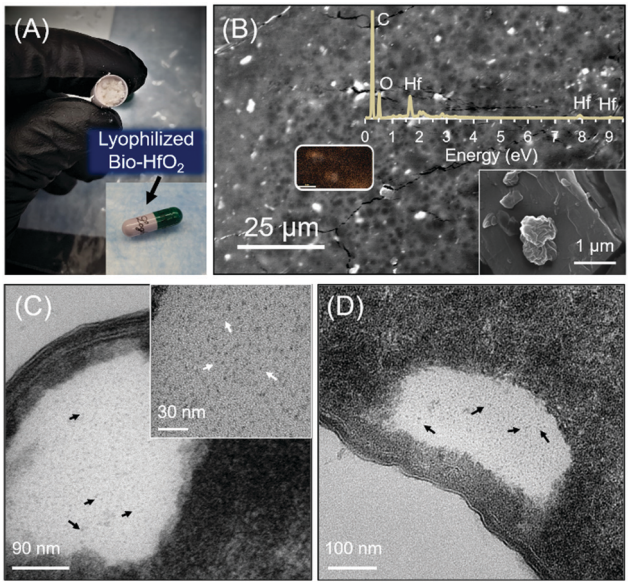

Fig. 5 (A) Packing of freeze-dried bacteria in a gelatin capsule (B) SEM of freeze-dried bacteria where the selected area (shown in rectangle) indicates the EDS map of Hf distribution, the top inset is the EDS spectrum while the bottom inset is a magnified region; the TEM images of bacteria incubated with NPs (C) *E. coli* Nissle and (D) *L. lactis*. The inset in (C) is well-dispersed TEM image of the shown region, arrows: P-HfO_2 NPs.

Furthermore, to make this method feasible for potential human application, we devised a strategy for their storage. We incubated *E. coli* Nissle with 10 mg ml^{-1} P-HfO_2 NPs as mentioned previously and then washed multiple times to remove the excess of NPs. Subsequently, the samples were freeze dried for further application using 10 wt% sucrose as lyoprotective media. As could be inferred from the EDS of the lyophilized bacteria, the binding energy of Hf is evident, hence confirming the internalization of P-HfO_2 NPs in the bacterial cells. Moreover, we revived the stored cells in the following days in the media and the cells indicated normal growth rate and OD_{600} reached to 2.09 after 24 h growth (Fig. S8, ESI†). This strategy can be useful for actual clinical setup, where the freeze-dried probiotic can be packed in a capsule for the facile oral administration by the patient. As a proof of concept, we packed the lyophilized bacteria in the gelatin capsule as shown in Fig. 5A which shows the potential means for the application of these NPs in the clinical settings.

Hf is a high atomic number material with a well-placed K-edge (65.5 keV) within the diagnostic X-ray energy range. Using Hf with spectral photon-counting CT generates high CT contrast due to a reasonable number of photons below and above its K-edge. Such spectrally effective imaging properties of Hf show its potential as a suitable element as contrast agents. MARS scanners use spectral photon counting detectors to divide conventional broad X-ray spectrum into multiple separate bins. The spectral information enables the identification and quantification of multiple materials simultaneously.[68]

A MARS scanner was used to assess the Hf spectral response. The scanner provides spectral and material images at high spatial resolution (~90 μm cubic voxel size). We used four energy counters in the charge summing mode which provides high energy resolution (between 3 to 5 keV FWHM).[69,70] A multi-material calibration phantom containing P-HfO_2 NPs, bone-like hydroxyapatite (HA), and lipid were scanned. The calibration data was used to produce the material images for both the phantom and the upcoming *in vivo* studies.[71,72]

The calibration phantom is shown in Fig. S9 (ESI†) and the corresponding material channels are shown in Fig. 6B; all four

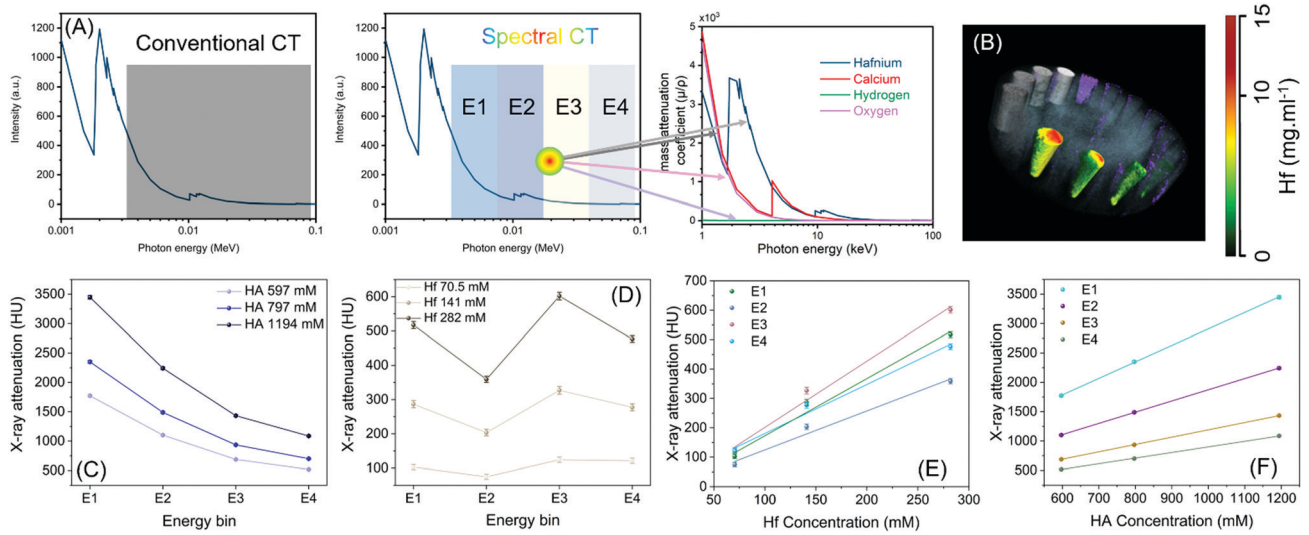

Fig. 6 (A) Comparison of conventional CT and spectral CT and the delineation of energy bins for 4 elements. The data are extracted from NIST database, X-ray attenuation properties of P-HfO_2 NPs; (B) material decomposed image of the phantom with water-equivalent material (blue), lipid (purple), Hf (green/yellow/red), HA (grey/white); spectral response of the detector for calibration vials for (C) HA rods and (D) P-HfO_2 NPs. E1, E2, E3, and E4 are 30–45, 45–65, 65–80, and 80–118 keV, respectively. Attenuation enhancement observed in energy bin 3 (65–80 keV) indicates the K-edge of Hf; 65.4 keV; Linearity of attenuation of (E) P-HfO_2 NPs and (F) HA.

materials are identified correctly in their calibration vials using the energy information. Examples of one CT slice from each energy bin are shown in Fig. S10 (ESI†). The spectral response for Hf and HA was graphically evaluated (Fig. 6C and D) and the linear correlation between attenuation and concentration across all four energy bins (Fig. 6E and F) was assessed. Fig. 6C shows the rise in attenuation in the third energy bin (65–80 keV) which corresponds to Hf's K-edge energy range, whereas no such response is observed for HA in Fig. 6B. Linear regression generated R^2 values very close to 1 for all lines suggesting a good fit. The accuracy of material identification and quantification is influenced by the linearity established for each energy bin, using the calibration vials.

Having established the CT attenuation properties of P-HfO_2 as well as their potential for application in spectral CT, we sought the application of bio-HfO_2 NPs as a contrast agent in conventional CT *in vivo*. For this experiment, the OD_{600} for *E. coli* Nissle was adjusted to 0.6 and then it was incubated with 54 mg of NPs for 4 h. The amount of Hf internalized by the probiotics was measured by Inductively coupled plasma – optical emission spectrometry (ICP-OES), calculated from the ICP standard curve generated for Hf (Fig. S11, ESI†) and tabulated in the Table S1 (ESI†). It was observed that internalized Hf concentration in the probiotics was 4.582 ppm. Separately, the incubated probiotic sample was lyophilized as detailed above. The formulation was resuspended in 1 ml of PBS and was then administered *via* oral gavage to Sprague Dawley rats using a flexible feeding tube. The rats were then imaged after 30 min GI tract are lighting up in the presence of the bio-HfO_2 (Fig. 7A). The internal organs namely intestine, caecum and small bowel diverticula were also observed. Interestingly, the contrast materials were detected in the rectum and anus (lower section) of the GI tract suggesting their fast clearance within 30 min. This experiment also indicated that the contrast agent can favorably withstand the various pH changes and harsh condition of the GI tract while avoiding the systemic absorption.

Fig. 7B and C show the one charge summing mode (CSM) energy bin of the rat without and with Hf material channel overlay, respectively. Fig. 7D shows the material images in 3D view and gives a clear indication of where P-HfO_2 NPs has accumulated *i.e.*, in the stomach/gut. Material decomposition showed Hf could be distinguished from bone (Fig. 7C) whereas, in the greyscale image, the bio-HfO_2 NPs appear like calcium (Fig. 7B).

In addition, we quantified the concentration of bio-HfO_2 (with reference to P-HfO_2 NPs) within the region of interest circled in Fig. 7D. These concentration values provide information to assess the NPs delivery. This dense region of Hf material within the GI tract was selected for quantification. By selecting the region of interest within several slides, Hf was quantified (Fig. S14, ESI†). The quantification of Hf in the stomach revealed that the concentration ranged between 2.79 and 447.0 mg ml^{-1}. The region was split into low, mid, and high concentrations. Several slices were selected and contoured according to min and max concentration (Fig. 7F). The resulting

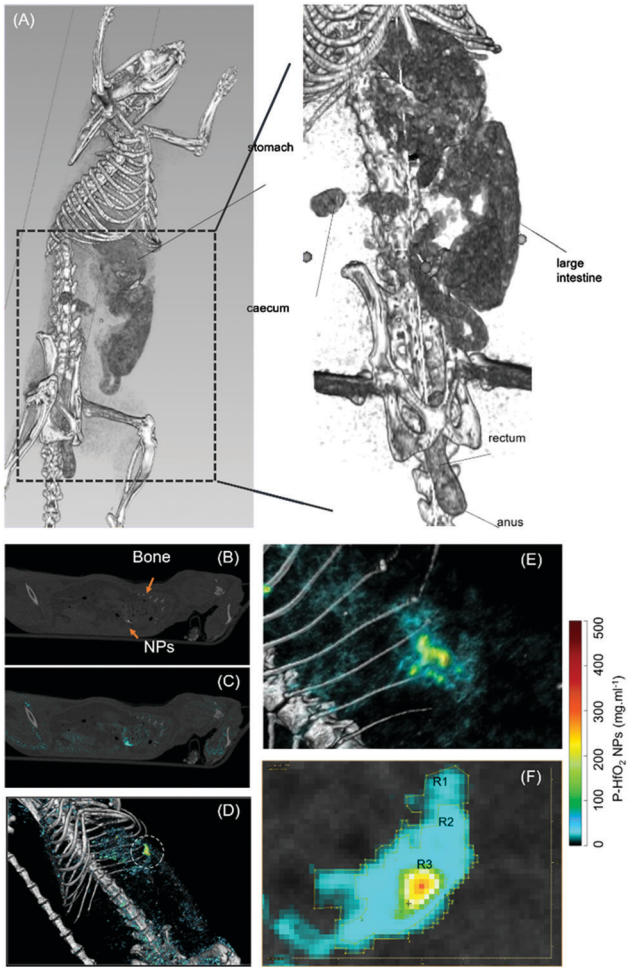

Fig. 7 (A) Representative 3D reconstruction of conventional CT image for rat gavage with bio-HfO_2; (B) coronal view from one energy bin of the rat which shows a bright area within the stomach region. (C) Coronal view with Hf material channel overlay with the energy bin channel. The bright area is associated with the presence of Hf solution while materials decomposition enables differentiation between Hf and bone; (D) 3D volumetric visualization of the material decomposition from the energy data. The region within the stomach that suggests a high presence of Hf is magnified (insert) and circled; (E) and (F) axial view of the region circled in (D). Measurements of Hf within this region were recorded. The 3D volume was split into three regions; R1, R2, and R3 which corresponds with low, mid, and high regions of concentration, respectively.

measurements are displayed in Table 1. The overall measurement (N = 6683) of Hf concentration was thus found to be a multi-modal distribution. Fig. S14a (ESI†) shows the distribution from one of these regions, which measured min, max, median, and mean. This experiment revealed the potential of bio-HfO_2 for quantitative assessments using spectral CT.

Thus, we have developed a novel microencapsulation technique where probiotics were proposed as an effective 'hitchhiker' to improve the survival, resistance, and targeted release of nanoparticle contrast materials in the GI tract. The inherent sensitivity of CT is low and therefore, high concentration of contrast materials must be used for *in vivo* bioimaging. The microencapsulation technique developed here would allow us

Table 1 Measurements of hafnium concentration from the dense region in the stomach, shown in Fig. 7E and F is the number of voxels selected from the biological sample. R1 measured a 3D volume excluding R2 and R3 and R2 excludes R3

	N	Min (mg ml^{-1})	Max (mg ml^{-1})	Mean (mg ml^{-1})
R1 (low)	3670	15	7	7
R2 (mid)	2479	78	30	30
R3 (high)	535	447	221	232
Overall	6683	3	11	35

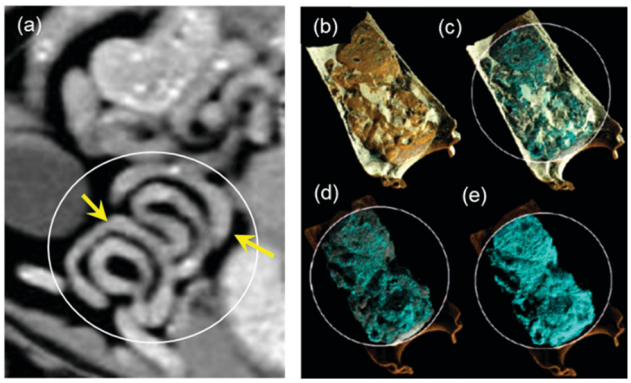

Fig. 8 Material-weighted photon counting CT images of the GI tract where the rats were fed before the gavage of probiotic-Hf capsule. (a) soft tissue (orange) and lipid (yellow); (b) lipid (yellow) and HfO_2 NPs (cyan); (c) HfO_2 NPs (cyan) and HA (gray) and (d) HfO_2 NPs (cyan).

for effective entrapment of high quantities of metallic nanoparticles within a biocompatible microenvironment that protects the particles from exposure to exterior factors (such as low gastric pH) during digestion, and subsequently to reduce cell injury or cell death before their release at the target site.

Proof-of-concept k-edge imaging study was also performed in an elaborate manner to compare conventional CT and spectral CT and the delineation of energy bins for 4 elements in phantoms. For *in vivo* study, material-weighted photon counting CT images of the GI tract was imaged and demonstrated to show unprecedented delineation of soft tissue, lipid, HA (calcium), which was absent in the conventional CT of the GI tract of a rat administered with iodine contrast agent (Fig. 7a and 8a). To demonstrate the transfer of the particles in the GI tract, we have also acquired multiple CT images to confirm the presence of hafnia nanoparticles. We have dissected the rat and excised its GI tract for imaging purposes. To demonstrate the clinical applicability of this technology, images without fasting before taking the probiotic-Hf capsule were acquired for the rats. Accordingly, the rats were fed before the gavage which means that there was food in the digestive organs, including the GI tract. It is known that most lab food provided to rats are calcium-rich,[73] then we can expect to detect food (calcium) in the HA channel. In this scenario, we used 4 basis vectors to run the Materials Decomposition (MD) algorithms in the spectral CT: Hf, HA (to represent Ca), lipid, and water. It was understood that from the calibration vials, there is a chance that low HfO_2 nanoparticle concentration can be misidentified as HA. But we have used quite a high amount of Hf during the experiment, *i.e.*, 54 mg of hafnia nanoparticle in 1 ml of PBS which was then administered *via* oral gavage to Sprague Dawley rats using a flexible feeding tube. Therefore, the majority of the voxels contain a high concentration of Hf, which means the chance of misidentification is significantly low. It also indicated the high transfer of nanoparticles to the lining of GI tract when probiotics were compressed through the GI tract. Thus, where conventional CT cannot make the distinction between Hf and calcium/mineral material in food, the spectral CT images can efficiently discriminate Hf signal from food signal. The data related to this study has been provided in (Fig. 8). We further evaluated *in vivo* toxicity of the synthesized nanoparticle on different clearance organs. As the nanoparticles were gavaged, the toxicity of the nanoparticles was evaluated on small intestine, colon, rectum, liver and kidney. However, no change on hematoxylin and eosin profile was found for all the tested organs indicating insignificant *in vivo* toxicity of the nanoparticles (Fig. S15, ESI†).

In conclusion, we designed ultra-small ($\sim$2 nm) P-HfO_2 NPs which were obtained *via* an ultrafast facile synthetic procedure. Subsequently, in a proof-of-concept study, we utilized the interface of nanomaterials and biological entities (probiotics) to pack and deliver GI contrast agents for the patient-friendly oral delivery. The NPs showed immense cytocompatibility in concentrations as high as 10 mg ml^{-1}. The CT imaging of the animal administered with these NPs promisingly indicated the details of GI tract. Interestingly, we could observe distinct contrast for P-HfO_2 NPs under *in vivo* conditions even in the fed state post 30 min of administration. Hence, we will take this opportunity to investigate the effect on contrast post P-HfO_2 NP administration *in vivo* at different time points through a separate full-blown study. In that future study, we will also monitor the time-dependent contrast and clearance of P-HfO_2 NPs under *in vivo* setting. The strategy indicated here can potentially be applied for a gamut of diseases such as cancer and cardiovascular diseases in the future. The scope of this present work is, however, to propose for the first time hitchhiking a probiotic vector to deliver high density hafnium nanodots for multicolor delineation of intestinal wall using photon counting CT. The translation of nanoparticle-based contrast probes consists of several stages from idea conceptualization, *in vitro* testing, preclinical testing in a small cohort of animals to final large-scale clinical trials. This current study majorly emphasizes the idea conceptualization more than any other stage and is a proof-of-concept study and for the full translation of this technology more preclinical evaluation will be warranted in the future. The complete translation of this technology does indeed require more in-depth studies which will be warranted in the follow up future studies.

Author contributions

D. P. conceived the idea. F. O. and D. P. designed the study. F. O., M. N., I. T. and S. K. M. performed the initial study and

developed the materials suitable for spectral C. T. C. L., M. M., A. B., N. R. and H. M. acquired the spectral C. T. scans. P. M. and N. G. contributed towards the revision of this manuscript by performing additional experiments to support the hypothesis. The manuscript was written through contributions of all authors. All authors have given approval to the final version of the manuscript. F. O. and P. M. contributed equally to this manuscript.

Funding sources

This work was financially supported by UIUC and NIH. FO gratefully acknowledge partial support from American heart association grant (#18pre34080003/2018) and Beckman institute postdoctoral fellowship.

Conflicts of interest

Prof. Pan is the founder or co-founder of three University based start ups. None of these entities however, supported this work. All the other authors declare no conflicts of interests.

Acknowledgements

Zeta potential, FTIR, TEM, XRD and XPS measurements were conducted at the Frederick Seitz Materials Research Laboratory, UIUC. The authors thank Dr Richard Haasch for help with the analysis and experiment for XPS studies. The authors also greatly thank help from veterinary medicine CT suit staff (Susan Hartman). We appreciate help from Dr Mauro Sardela for carrying our XRD experiment.

References

1 J. Keller, G. Bassotti, J. Clarke, P. Dinning, M. Fox, M. Grover, P. M. Hellström, M. Ke, P. Layer and C. Malagelada, *Nat. Rev. Gastroenterol. Hepatol.*, 2018, **15**, 291.
2 J. Burggraaf, I. M. Kamerling, P. B. Gordon, L. Schrier, M. L. De Kam, A. J. Kales, R. Bendiksen, B. Indrevoll, R. M. Bjerke and S. A. Moestue, *Nat. Med.*, 2015, **21**, 955.
3 X. Yang, J. F. Lovell and Y. Zhang, *ChemBioChem*, 2019, **20**, 462–473.
4 Q. Cheng, H. Shi, H. Huang, Z. Cao, J. Wang and Y. Liu, *Chem. Commun.*, 2015, **51**, 17536–17539.
5 M. W. Tibbitt, J. E. Dahlman and R. Langer, *J. Am. Chem. Soc.*, 2016, **138**, 704–717.
6 D. Pan, M. Pramanik, S. A. Wickline, L. V. Wang and G. M. Lanza, *Contrast Media Mol. Imaging*, 2011, **6**, 378–388.
7 P. Mukherjee, S. K. Misra, M. C. Gryka, H.-H. Chang, S. Tiwari, W. L. Wilson, J. W. Scott, R. Bhargava and D. Pan, *Small*, 2015, **11**, 4691–4703.
8 E. M. Pridgen, F. Alexis, T. T. Kuo, E. Levy-Nissenbaum, R. Karnik, R. S. Blumberg, R. Langer and O. C. Farokhzad, *Sci. Transl. Med.*, 2013, **5**, 213ra167.
9 S. Mitragotri, P. A. Burke and R. Langer, *Nat. Rev. Drug Discovery*, 2014, **13**, 655–672.
10 R. Wang, L. Zhou, W. Wang, X. Li and F. Zhang, *Nat. Commun.*, 2017, **8**, 14702.
11 C. T. N. Pham, D. G. Thomas, J. Beiser, L. M. Mitchell, J. L. Huang, A. Senpan, G. Hu, M. Gordon, N. A. Baker, D. Pan, G. M. Lanza and D. E. Hourcade, *Nanomedicine*, 2014, **10**, 651–660.
12 D. Pan, M. Pramanik, A. Senpan, S. A. Wickline, L. V. Wang and G. M. Lanza, *J. Nanosci. Nanotechnol.*, 2010, **10**, 8118–8123.
13 D. Akin, J. Sturgis, K. Ragheb, D. Sherman, K. Burkholder, J. P. Robinson, A. K. Bhunia, S. Mohammed and R. Bashir, *Nat. Nanotechnol.*, 2007, **2**, 441.
14 M. H. Ross, A. K. Esser, G. C. Fox, A. H. Schmieder, X. Yang, G. Hu, D. Pan, X. Su, Y. Xu, D. V. Novack, T. Walsh, G. A. Colditz, G. H. Lukaszewicz, E. Cordell, J. Novack, J. A. J. Fitzpatrick, D. L. Waning, K. S. Mohammad, T. A. Guise, G. M. Lanza and K. N. Weilbaecher, *Cancer Res.*, 2017, **77**, 6299–6312.
15 M. S. Khan, S. K. Misra, K. Dighe, Z. Wang, A. S. Schwartz-Duval, D. Sar and D. Pan, *Biosens. Bioelectron.*, 2018, **110**, 132–140.
16 R. H. Fang, A. V. Kroll, W. Gao and L. Zhang, *Adv. Mater.*, 2018, **30**, 1706759.
17 D. Pan, A. H. Schmieder, K. Wang, X. Yang, A. Senpan, G. Cui, K. Killgore, B. Kim, J. S. Allen, H. Zhang, S. D. Caruthers, B. Shen, S. A. Wickline and G. M. Lanza, *Theranostics*, 2014, **4**, 565–578.
18 F. Ostadhossein and D. Pan, *Wiley Interdiscip. Rev.: Nanomed. Nanobiotechnol.*, 2017, **9**, e1436.
19 O. Felfoul, M. Mohammadi, S. Taherkhani, D. De Lanauze, Y. Z. Xu, D. Loghin, S. Essa, S. Jancik, D. Houle and M. Lafleur, *Nat. Nanotechnol.*, 2016, **11**, 941.
20 M. Mahmoudi, N. Bertrand, H. Zope and O. C. Farokhzad, *Nano Today*, 2016, **11**, 817–832.
21 I. Srivastava, S. K. Misra, F. Ostadhossein, E. Daza, J. Singh and D. Pan, *Nano Res.*, 2017, **10**, 3269–3284.
22 M. S. Khan, K. Dighe, Z. Wang, I. Srivastava, E. Daza, A. S. Schwartz-Dual, J. Ghannam, S. K. Misra and D. Pan, *The Analyst*, 2018, **143**, 1094–1103.
23 S. K. Misra, H.-H. Chang, P. Mukherjee, S. Tiwari, A. Ohoka and D. Pan, *Sci. Rep.*, 2015, **5**, 14986.
24 D. Pan, *Mol. Pharmaceutics*, 2013, **10**, 781–782.
25 S. K. Misra, F. Ostadhossein, E. Daza, E. V. Johnson and D. Pan, *Adv. Funct. Mater.*, 2016, **26**, 8031–8041.
26 M. A. Dobrovolskaia and S. E. McNeil, *Nat. Nanotechnol.*, 2007, **2**, 469.
27 B. Illes, P. Hirschle, S. Barnert, V. Cauda, S. Wuttke and H. Engelke, *Chem. Mater.*, 2017, **29**, 8042–8046.
28 M. Goldberg and I. Gomez-Orellana, *Nat. Rev. Drug Discovery*, 2003, **2**, 289.
29 G. Traverso and R. Langer, *Nature*, 2015, **519**, S19.
30 Z. Wu, L. Li, Y. Yang, P. Hu, Y. Li, S.-Y. Yang, L. V. Wang and W. Gao, *Sci. Robotics*, 2019, **4**, eaax0613.
31 G. Iddan, G. Meron, A. Glukhovsky and P. Swain, *Nature*, 2000, **405**, 417.
32 Z. Liu, X. Ran, J. Liu, Y. Du, J. Ren and X. Qu, *Biomaterials*, 2016, **100**, 17–26.

33 D. Pan, E. Roessl, J. P. Schlomka, S. D. Caruthers, A. Senpan, M. J. Scott, J. S. Allen, H. Zhang, G. Hu and P. J. Gaffney, *Angew. Chem., Int. Ed.*, 2010, **49**, 9635–9639.
34 D. Pan, C. O. Schirra, A. Senpan, A. H. Schmieder, A. J. Stacy, E. Roessl, A. Thran, S. A. Wickline, R. Proska and G. M. Lanza, *ACS Nano*, 2012, **6**, 3364–3370.
35 D. P. Cormode, S. Si-Mohamed, D. Bar-Ness, M. Sigovan, P. C. Naha, J. Balegamire, F. Lavenne, P. Coulon, E. Roessl, M. Bartels, M. Rokni, I. Blevis, L. Boussel and P. Douek, *Sci. Rep.*, 2017, **7**, 4784.
36 R. K. Panta, A. P. Butler, P. H. Butler, N. J. de Ruiter, S. T. Bell, M. F. Walsh, R. M. Doesburg, A. I. Chernoglazov, B. P. Goulter and P. Carbonez, *IEEE Nuclear Science Symposium and Medical Imaging Conference Proceedings (NSS/MIC)*, 2018, p 1.
37 K. Taguchi and J. S. Iwanczyk, *Med. Phys.*, 2013, **40**, 100901.
38 S. A. Si-Mohamed, J. Miailhes, P.-A. Rodesch, S. Boccalini, H. Lacombe, V. Leitman, V. Cottin, L. Boussel and P. Douek, *J. Clin. Med.*, 2021, **10**, 5757.
39 M. J. Willemink, M. Persson, A. Pourmorteza, N. J. Pelc and D. Fleischmann, *Radiology*, 2018, **289**, 293–312.
40 J. Balegamire, M. Vandamme, E. Chereul, S. Si-Mohamed, S. A. Maache, E. Almouazen, L. Ettouati, H. Fessi, L. Boussel and P. Douek, *Biomater. Sci.*, 2020, **8**, 5715–5728.
41 M. A. Kimm, M. Shevtsov, C. Werner, W. Sievert, W. Zhiyuan, O. Schoppe, B. H. Menze, E. J. Rummeny, R. Proksa and O. Bystrova, *Cancers*, 2020, **12**, 1331.
42 X. Meng, Y. Wu and W. Bu, *Adv. Healthcare Mater.*, 2020, 2000912.
43 F. Ostadhossein, I. Tripathi, L. Benig, D. LoBato, M. Moghiseh, C. Lowe, A. Raja, A. Butler, R. Panta and M. Anjomrouz, *Adv. Funct. Mater.*, 2020, **30**, 1904936.
44 X. Wang, J. Wang, J. Pan, F. Zhao, D. Kan, R. Cheng, X. Zhang and S.-K. Sun, *ACS Appl. Mater. Interfaces*, 2019, **11**, 33650–33658.
45 S. Si-Mohamed, D. P. Cormode, D. Bar-Ness, M. Sigovan, P. C. Naha, J.-B. Langlois, L. Chalabreysse, P. Coulon, I. Blevis, E. Roessl, K. Erhard, L. Bousselab and P. Douek, *Nanoscale*, 2017, **9**, 18246–18257.
46 W. Liao, P. Lei, J. Pan, C. Zhang, X. Sun, X. Zhang, C. Yu and S.-K. Sun, *Biomaterials*, 2019, **203**, 1–11.
47 M. W. Galper, M. T. Saung, V. Fuster, E. Roessl, A. Thran, R. Proska, Z. A. Fayad and D. P. Cormode, *Invest Radiol.*, 2012, **47**, 475–481.
48 A. Saraste, S. G. Nekolla and M. Schwaiger, *Cardiovasc. Res.*, 2009, **83**, 643–652.
49 L. Ren, N. Huber, K. Rajendran, J. G. Fletcher, C. H. McCollough and L. Yu, *Invest. Radiol.*, 2022, **57**, 122–129.
50 M. Moghiseh, C. Lowe, J. G. Lewis, D. Kumar, A. Butler, N. Anderson and A. Raja, *Contrast Media Mol. Imaging*, 2018, 2136840.
51 M. Getzin, J. J. Garfield, D. S. Rundle, U. Kruger, A. P. H. Butler, M. Gkikas and G. Wang, *J. X-Ray Sci. Technol.*, 2018, **26**, 707–726.
52 S. A. Si-Mohamed, M. Sigovan, J. C. Hsu, V. Tatard-Leitman, L. Chalabreysse, P. C. Naha, T. Garrivier, R. Dessouky, M. Carnaru, L. Boussel, D. P. Cormode and P. C. Douek, *Radiology*, 2021, **300**, 98–107.
53 P. C. Naha, J. C. Hsu, J. Kim, S. Shah, M. Bouché, S. Si-Mohamed, D. N. Rosario-Berrios, P. Douek, M. Hajfathalian, P. Yasini, S. Singh, M. A. Rosen, M. A. Morgan and D. P. Cormode, *ACS Nano*, 2020, **14**, 10187–10197.
54 C. Kramer, *Circulation*, 2008, **117**, 1333–1339.
55 P. A. Jackson, W. N. W. A. Rahman, C. J. Wong, T. Ackerly and M. Geso, *Eur. J. Radiol*, 2010, **75**, 104–109.
56 S. Zhang, R. Langer and G. Traverso, *Nano Today*, 2017, **16**, 82–96.
57 Z. Zhou, X. Chen, H. Sheng, X. Shen, X. Sun, Y. Yan, J. Wang and Q. Yuan, *Microbial Cell Factories*, 2020, **19**, 56.
58 D. Pan, A. H. Schmieder, A. SenPan, X. Yang, S. A. Wickline, E. Roessl, R. Proksa, C. O. Schirra and G. M. Lanza, *Design and Applications of Nanoparticles in Biomedical Imaging*, Springer, 2017, pp. 385–402.
59 T. Danino, A. Prindle, G. A. Kwong, M. Skalak, H. Li, K. Allen, J. Hasty and S. N. Bhatia, *Sci. Transl. Med.*, 2015, **7**, 289ra84.
60 J. Suez, N. Zmora, E. Segal and E. Elinav, *Nat. Med.*, 2019, **25**, 716–729.
61 F. Ostadhossein, S. K. Misra, I. Tripathi, V. Kravchuk, G. Vulugundam, D. LoBato, L. E. Selmic and D. Pan, *Biomaterials*, 2018, **181**, 252–267.
62 S. Bonvalot, P. L. Rutkowski, J. Thariat, S. Carrère, A. Ducassou, M.-P. Sunyach, P. Agoston, A. Hong, A. Mervoyer and M. Rastrelli, *The Lancet Oncology*, 2019, **20**, 1148–1159.
63 F. Ostadhossein, I. Tripathi, L. Benig, D. LoBato, M. Moghiseh, C. Lowe, A. Raja, A. Butler, R. Panta and M. Anjomrouz, *Adv. Funct. Mater.*, 2020, **30**, 1904936.
64 T. L. McGinnity, O. Dominguez, T. E. Curtis, P. D. Nallathamby, A. J. Hoffman and R. K. Roeder, *Nanoscale*, 2016, **8**, 13627–13637.
65 L. R. Gerken, K. Keevend, Y. Zhang, F. H. Starsich, C. Eberhardt, G. Panzarasa, M. T. Matter, A. Wichser, A. Boss and A. Neels, *ACS Appl. Mater. interfaces*, 2018, **11**, 437–448.
66 O. Dominguez, T. L. McGinnity, R. K. Roeder and A. J. Hoffman, *Appl. Phys. Lett.*, 2017, **111**, 011101.
67 S.-J. Choi and J.-S. Choi, *Biomol. Ther.*, 2010, **18**, 469–476.
68 N. G. Anderson and A. P. Butler, *Contrast Media Mol. Imaging*, 2014, **9**, 3–12.
69 R. Ballabriga, M. Campbell, E. Heijne, X. Llopart and L. Tlustos, *IEEE Trans. Nuclear Sci.*, 2007, **54**, 1824–1829.
70 R. Ballabriga, J. Alozy, G. Blaj, M. Campbell, M. Fiederle, E. Frojdh, E. Heijne, X. Llopart, M. Pichotka and S. Procz, *J. Instrumentation*, 2013, **8**, C02016.
71 C. Bateman, *Methods for Material Discrimination in MARS Multi-energy CT*, PhD thesis, University of Otago, Christchurch, New Zealand, 2015.
72 C. Bateman, D. Knight, B. Brandwacht, J. Mc Mahon, J. Healy, R. Panta, R. Aamir, K. Rajendran, M. Moghiseh and M. Ramyar, *J. Instrumentation*, 2018, **13**, P05020.
73 S. M. Lewis, D. E. Ullrey, D. E. Barnard and J. J. Knapka, *American College of Laboratory Animal Medicine, The Laboratory Rat*, 2nd edn, 2006, pp. 219–301.

